Supplemental Materials for: Promoting Reversibility of Multielectron Redox in Alkali-Rich Sulfide Cathodes through Cryomilling

Seong Shik Kim,[†] David N. Agyeman-Budu,[‡] Joshua J. Zak,[†] Andrew Dawson,[¶] Qizhang Yan,[§] Miguel Cában-Acevedo,[†] Kamila M. Wiaderek,[∥] Andrey A. Yakovenko,[∥] Yiyi Yao,[¶] Ahamed Irshad,[⊥] Sri R. Narayan,[⊥] Jian Luo,[§] Johanna Nelson Weker,[‡] Sarah H. Tolbert,[¶] and Kimberly A. See[*,†]

†*Division of Chemistry and Chemical Engineering, California Institute of Technology, Pasadena, California 91125, United States*

‡*Stanford Synchrotron Radiation Lightsource, SLAC National Accelerator Laboratory, Menlo Park, California 94025, United States*

¶*Department of Chemistry and Biochemistry, University of California, Los Angeles, Los Angeles, California 90095, United States*

§*Department of NanoEngineering, University of California San Diego, La Jolla, California 92093, United States*

∥*Advanced Photon Source, Argonne National Laboratory, Lemont, IL, 60439, USA*

⊥*Department of Chemistry and Loker Hydrocarbon Research Institute, University of Southern California, Los Angeles, California 90089-1661, United States*

E-mail: ksee@caltech.edu

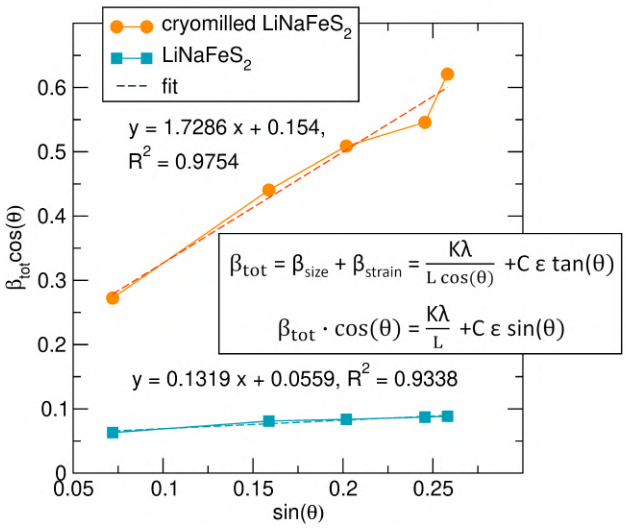

Figure S1: Williamson-Hall analysis of XRD peaks of as-prepared $LiNaFeS_2$ and cryomilled $LiNaFeS_2$. Calculated crystallite size decreases from 1.47 nm to 0.56 nm upon cryomilling, while microstrain increases from 29800 to 425500.

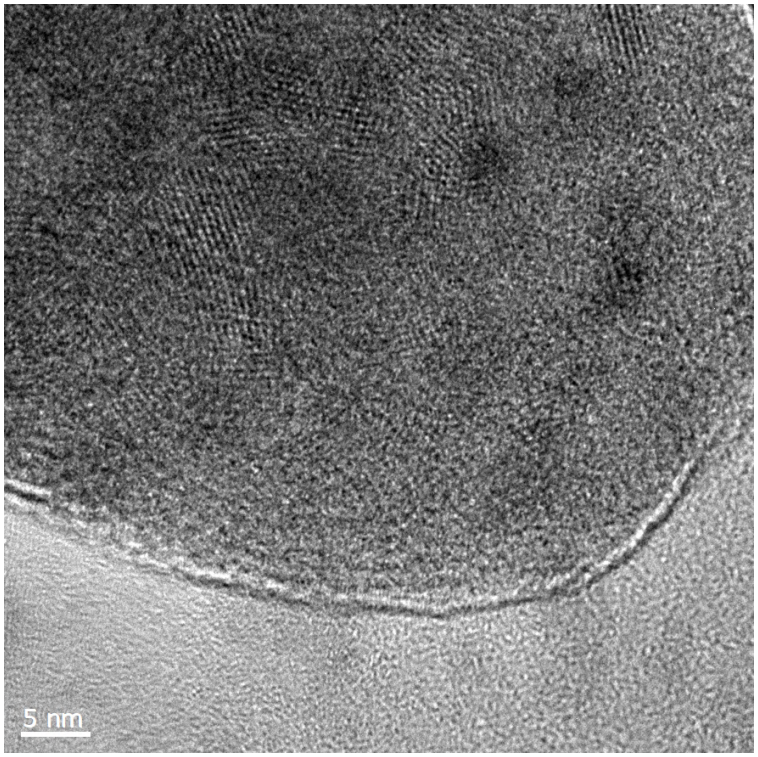

Figure S2: TEM image of as-prepared $LiNaFeS_2$. Regions of fringes are observed throughout the particle suggesting high crystallinity.

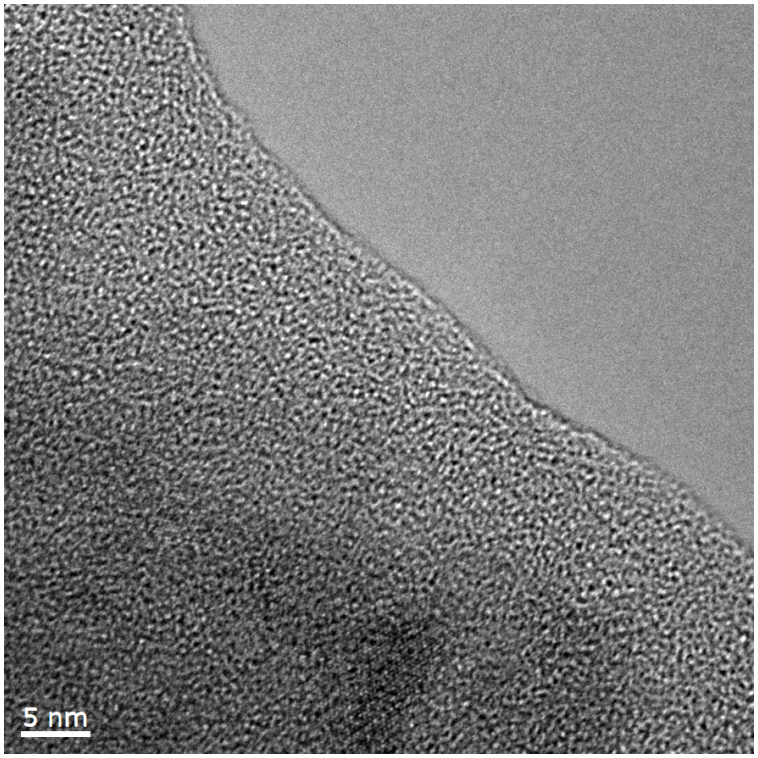

Figure S3: TEM image of cryomilled $LiNaFeS_2$. Fewer crystalline domains are observed, which only exist in the bulk. The surface of the particle appears amorphous.

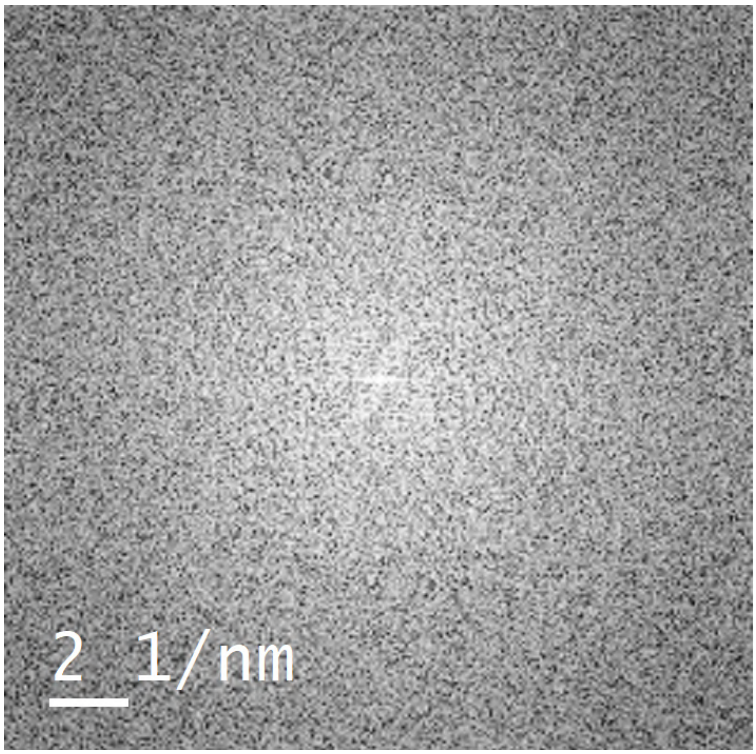

Figure S4: FFT of background carbon. The absence of a broad ring suggests that the broad ring observed in the FFT of the edge of cryomilled particle cannot be explained by carbon supporta lone.

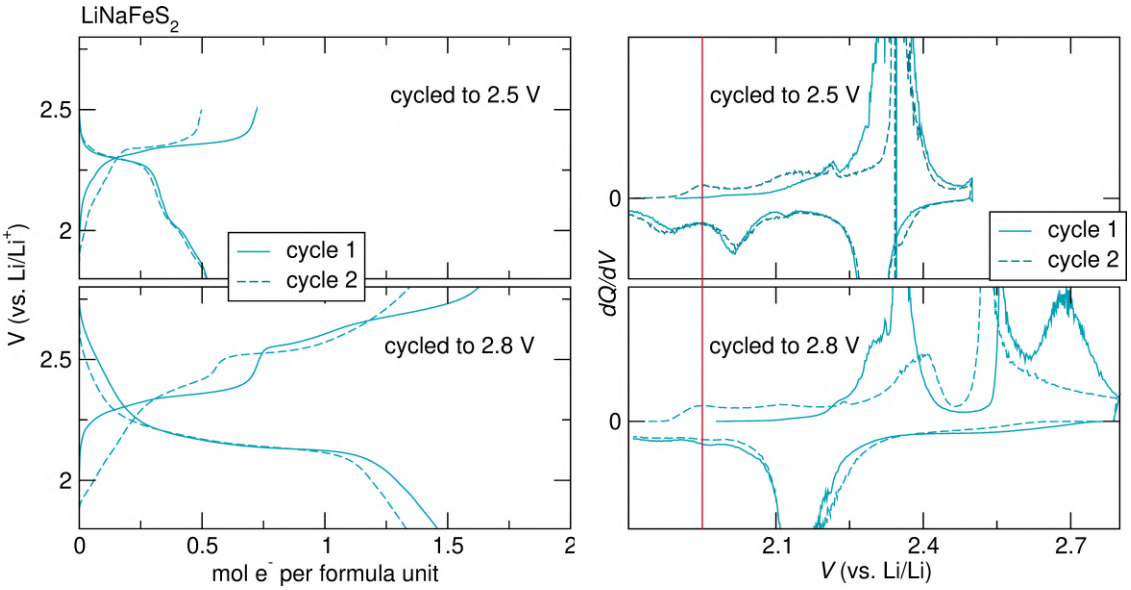

Figure S5: Galvanostatic cycling and corresponding dQ/dV plots of as-prepared $LiNaFeS_2$ to different upper voltage cutoffs 2.5 V and 2.8 V. Both upper cutoffs exhibit the same peak in the dQ/dV plots of cycle 2.

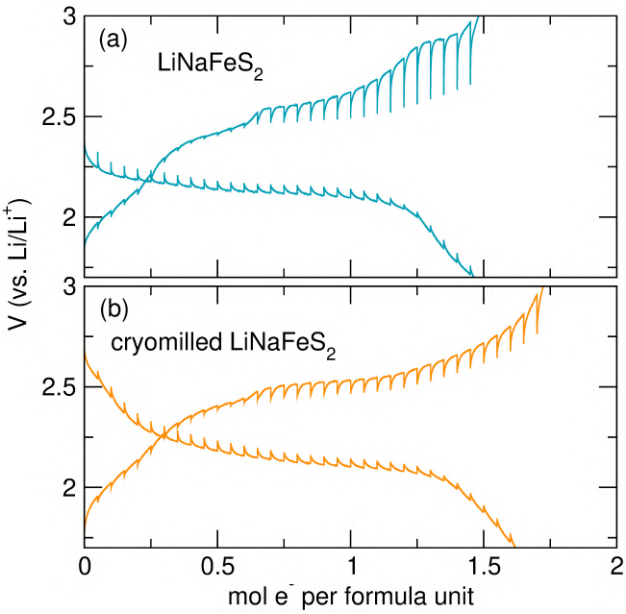

Figure S6: Cycle 13 GITT of (a) as-prepared $LiNaFeS_2$ and (b) cryomilled $LiNaFeS_2$. As-prepared $LiNaFeS_2$ continues to show higher overpotentials above 2.5 V.

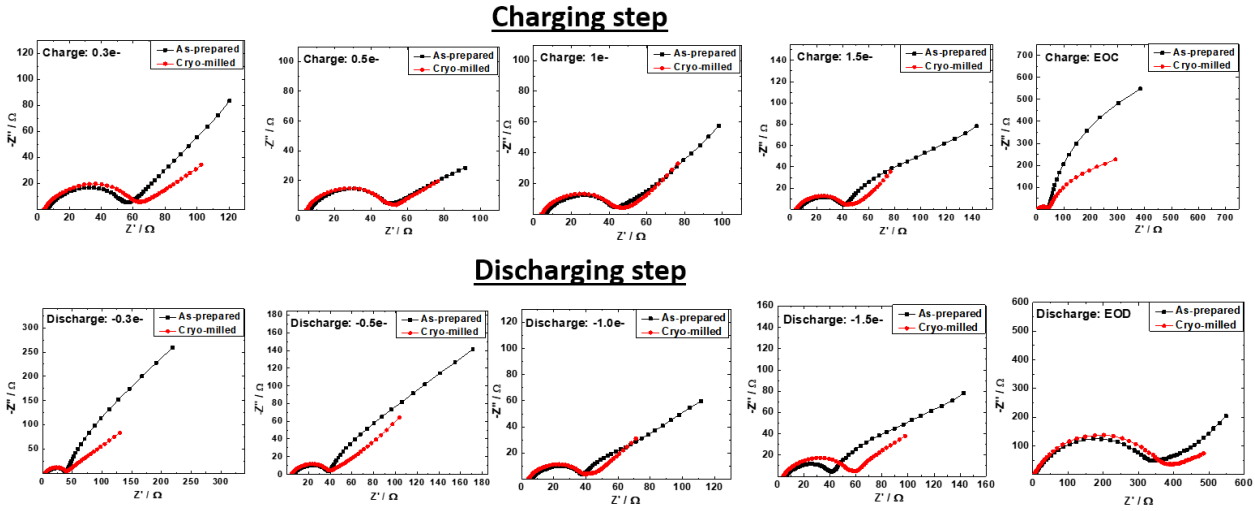

Figure S7: Intermittent EIS during cycle 1 at different states of charge. While high-frequency x-intercepts and the size of semicircles are similar, cryomilled $LiNaFeS_2$ always shows shorter tails, suggesting lower mass transfer resistance.

$$D = \frac{R^2T^2}{2A^2n^2F^4C^2\sigma^2}$$

Before cycling

$$(D_{Li+})_{cryo\text{-}milled} / (D_{Li+})_{as\text{-}prepared} = (\sigma^2)_{as\text{-}prepared} / (\sigma^2)_{cryo\text{-}milled}$$
$$= (120.01)^2 / (53.52)^2$$
$$= 5$$

0.5 e^- removed

$$(D_{Li+})_{cryo\text{-}milled} / (D_{Li+})_{as\text{-}prepared} = (\sigma^2)_{as\text{-}prepared} / (\sigma^2)_{cryo\text{-}milled}$$
$$= (22.89)^2 / (13.59)^2$$
$$= 2.8$$

Figure S8: Ratios of diffusion coefficients of as-prepared $LiNaFeS_2$ and cryomilled $LiNaFeS_2$ before cycling and 0.5 e^- removed assuming constant surface area. Cryomilled $LiNaFeS_2$ shows higher diffusion coefficients compared to as-prepared $LiNaFeS_2$.

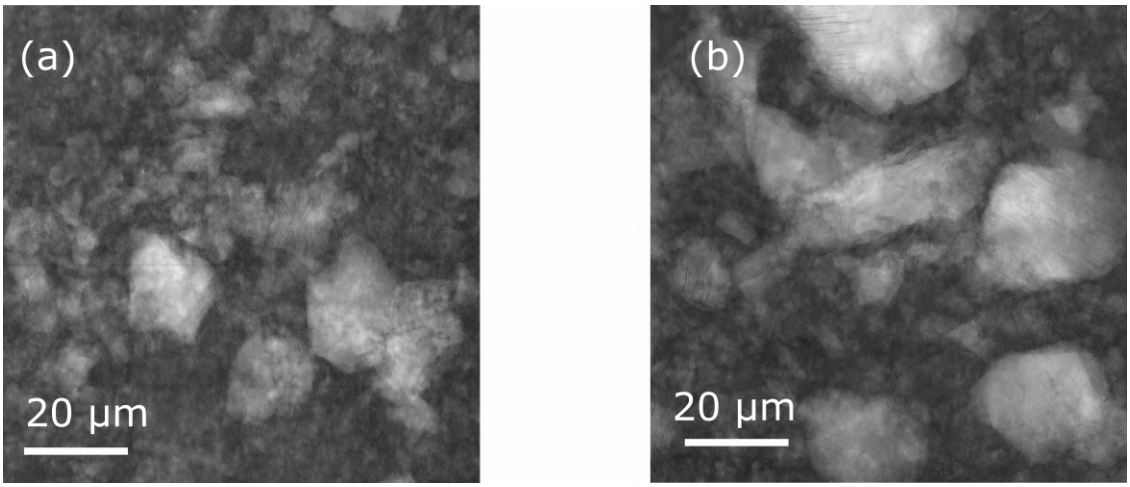

Figure S9: TXM mosaic micrographs of as-prepared $LiNaFeS_2$ (a) charged to 2.5 V, (b) fully charged to 3 V. Scale bars represent 20 μm. Particle fractures appear at 2.5 V, and more particle fractures are observed at the end of charge.

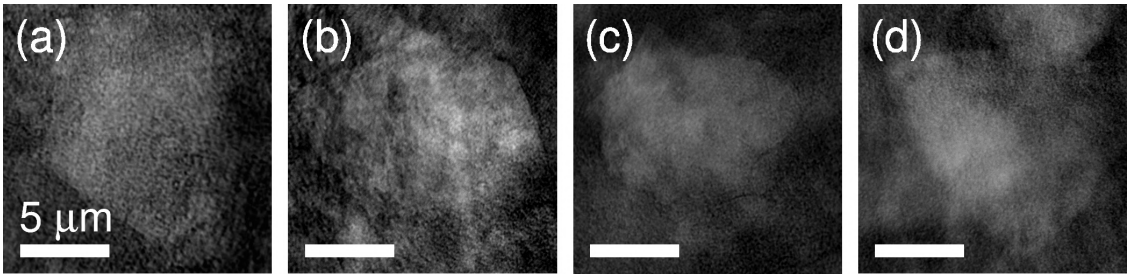

Figure S10: TXM micrographs of Li_2FeS_2 (a) before cycling, (b) charged to 2.5 V, (c) charged to 3 V, and (d) discharged to 1.7 V. Scale bars represent 5 μm. Li_2FeS_2 does not show signs of fracturing in all states of charge.

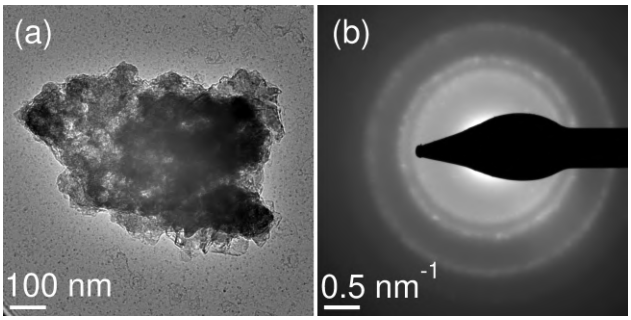

Figure S11: (a) Particle clusters of cryomilled $LiNaFeS_2$ and (b) diffraction rings in the corresponding selected area electron diffraction (SAED) pattern. The cluster is composed of small single crystalline particles that are randomly oriented.

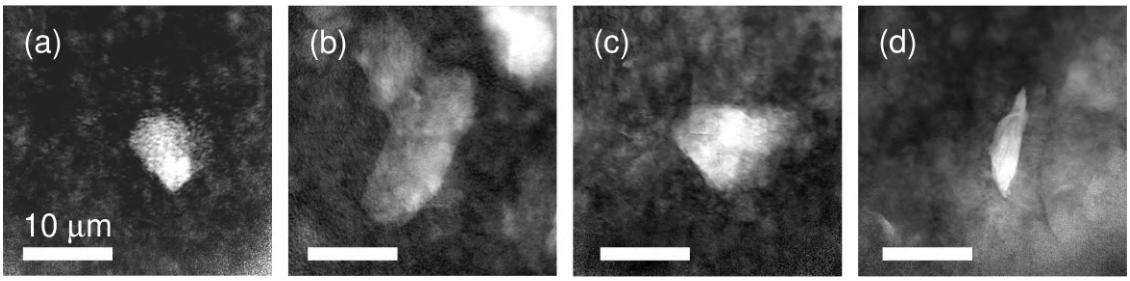

Figure S12: TXM micrographs of cryomilled $LiNaFeS_2$ (a) before cycling, (b) charged to 2.5 V, (c) charged to 3 V, and (d) charged to 3V then discharged to 1.7 V. Scale bars represent 10 μm. There are more smaller particles than bigger aggreagates. Brightness and contrast levels are adjusted so that smaller particles can be seen better.

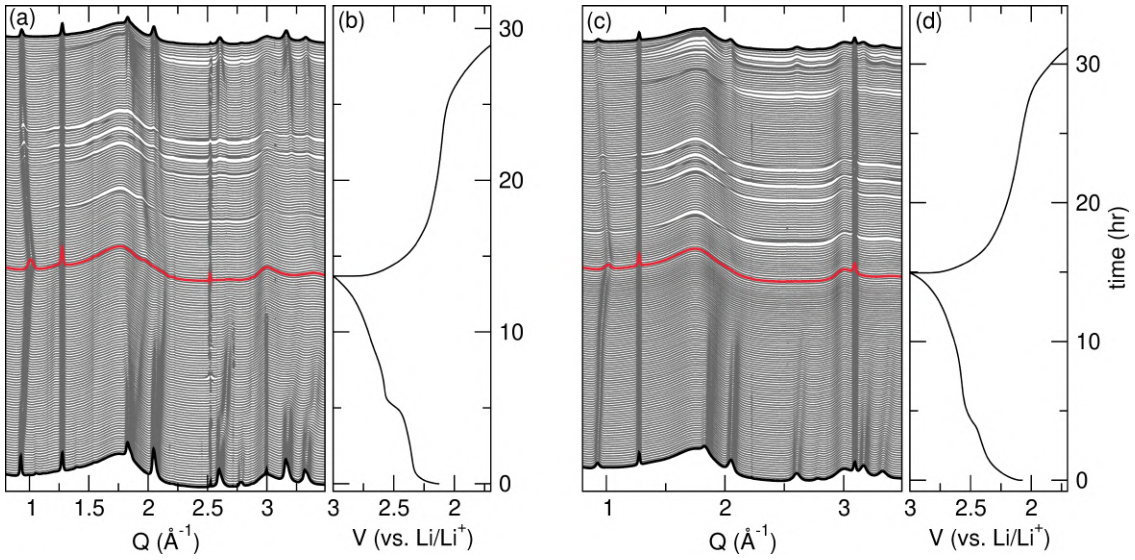

Figure S13: *Operando* sXRD of (a and b) as-prepared $LiNaFeS_2$ and (c and d) cryomilled $LiNaFeS_2$. The peak at 1.26 Q corresponds to PTFE binder.

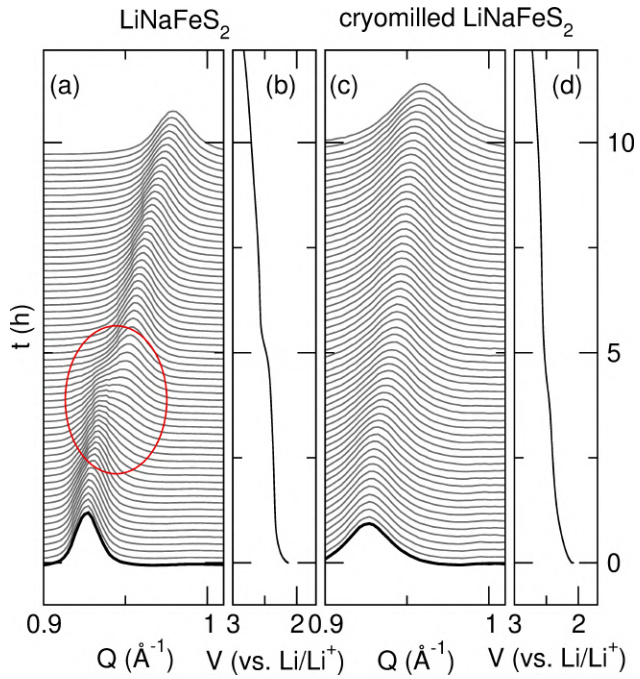

Figure S14: *Operando* sXRD of (a and b) as-prepared $LiNaFeS_2$ and (c and d) cryomilled $LiNaFeS_2$ magnified up to the first 10 hours of charge to highlight the new peak in as-prepared $LiNaFeS_2$.

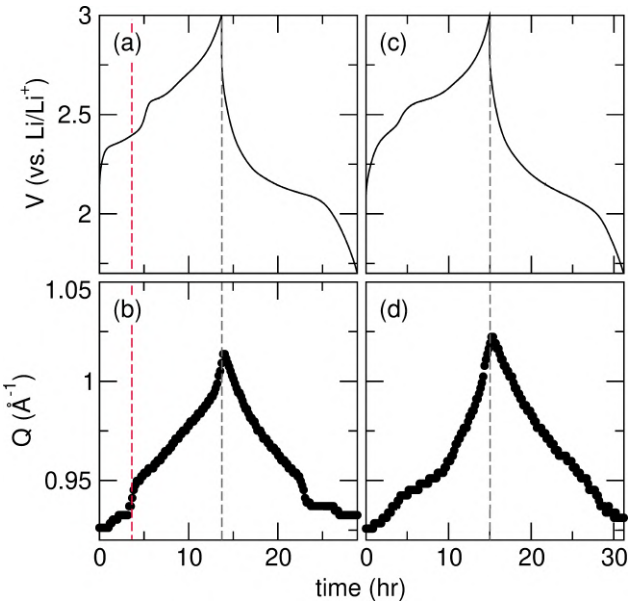

Figure S15: (a) Galvanostatic cycling data of as-prepared $LiNaFeS_2$ and (b) Q of the (001) reflection, and (c and d) corresponding data for cryomilled $LiNaFeS_2$. While both materials' (001) peaks reach the same Q and thus d-spacing at the end of charge, as-prepared $LiNaFeS_2$ exhibits a jump in Q suggesting a two-phase mechanism.

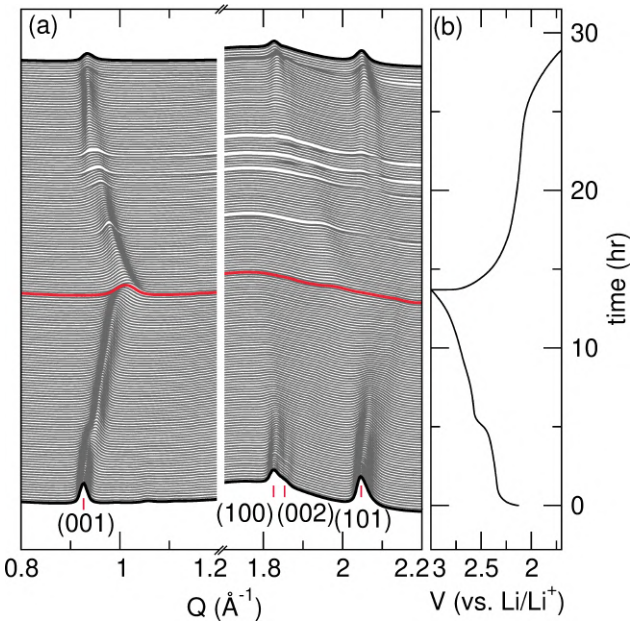

Figure S16: (a) *Operando* sXRD of as-prepared $LiNaFeS_2$ of selected Q regions and (b) the corresponding galvanostatic cycling data.

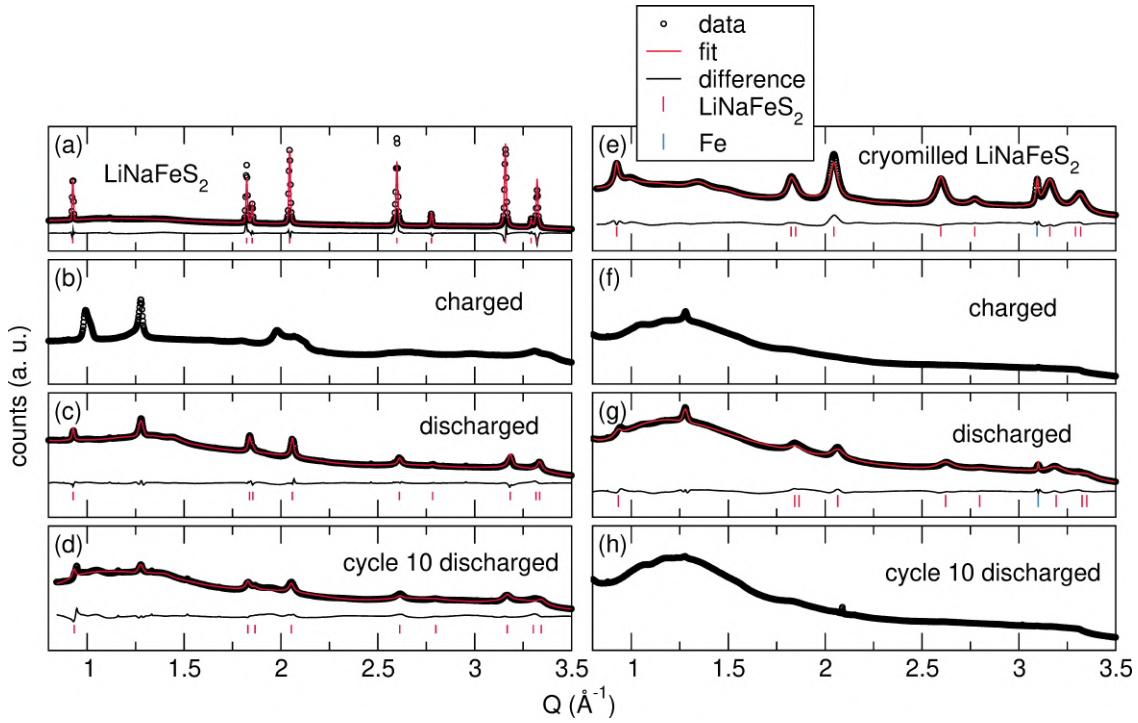

Figure S17: *Ex situ* sXRD of (a–d) as-prepared $LiNaFeS_2$ and (e–h) cryomilled $LiNaFeS_2$ at different states of charge. The peak at 1.26 Q corresponds to PTFE. While intensity attenuation of cryomilled $LiNaFeS_2$ precludes further analysis, diffraction patterns of discharged and cycle 10 discharged as-prepared $LiNaFeS_2$ can be fit with Rietveld refinement.